

# A pseudo-spectrum analysis of galaxy-galaxy lensing

Chiaki Hikage<sup>1</sup> and Masamune Oguri<sup>2,3,1</sup>

<sup>1</sup> *Kavli Institute for the Physics and Mathematics of the Universe (Kavli IPMU, WPI), The University of Tokyo, Kashiwa, Chiba 277-8583, Japan*

<sup>2</sup> *Research Center for the Early Universe, University of Tokyo, 7-3-1 Hongo, Bunkyo-ku, Tokyo 113-0033, Japan*

<sup>3</sup> *Department of Physics, University of Tokyo, 7-3-1 Hongo, Bunkyo-ku, Tokyo 113-0033, Japan*

6 October 2018

## ABSTRACT

We present the application of the pseudo-spectrum method to galaxy-galaxy lensing. We derive explicit expressions for the pseudo-spectrum analysis of the galaxy-shear cross spectrum, which is the Fourier space counterpart of the stacked galaxy-galaxy lensing profile. The pseudo-spectrum method corrects observational issues such as the survey geometry, masks of bright stars and their spikes, and inhomogeneous noise, which distort the spectrum and also mix the E-mode and the B-mode signals. Using ray-tracing simulations in  $N$ -body simulations including realistic masks, we confirm that the pseudo-spectrum method successfully recovers the input galaxy-shear cross spectrum. We also investigate the covariance of the galaxy-shear cross spectrum using the ray-tracing simulations to show that there is an excess covariance relative to the Gaussian covariance at small scales ( $k \gtrsim 1h/\text{Mpc}$ ) where the shot noise is dominated in the Gaussian approximation. We find that the excess of the covariance is consistent with the expectation from the halo sample variance (HSV), which originates from the matter fluctuations at scales larger than the survey area. We apply the pseudo-spectrum method to the observational data of Canada-France-Hawaii Telescope Lensing survey (CFHTLenS) shear catalogue and three different spectroscopic samples of Sloan Digital Sky Survey Luminous Red Galaxy (SDSS LRG), and Baryon Oscillation Spectroscopic Survey (BOSS) CMASS and LOWZ galaxies. The galaxy-shear cross spectra are significantly detected at the level of  $7 - 10\sigma$  using the analytic covariance with the HSV contribution included. We also confirm that the observed spectra are consistent with the halo model predictions with the halo occupation distribution parameters estimated from previous work. This work demonstrates the viability of galaxy-galaxy lensing analysis in the Fourier space.

**Key words:** cosmology: theory – observations – large-scale structure of the Universe – gravitational lensing: weak – methods: statistical

## 1 INTRODUCTION

Growth of large-scale structure probed by weak gravitational lensing and galaxy clustering provides a key insight into the nature of dark energy and dark matter. Galaxy-galaxy lensing, the cross-correlation between foreground galaxies and background galaxy image distortions, is a powerful probe of how the matter distributes around galaxies. Specifically, galaxy-galaxy lensing has been applied to various galaxy datasets to study the relation between galaxy properties and their host dark matter properties (e.g., Hoekstra et al. 2005; Mandelbaum et al. 2006; Leauthaud et al. 2012; Velander et al. 2014; Coupon et al. 2015). This relation, when combined with galaxy clustering measurements, reduces the systematic uncertainty of galaxy biasing and allows us to derive useful cosmological constraints (e.g., Mandelbaum et al. 2013; Miyatake et al. 2015; More et al. 2015). These applications will grow in the near future when high-quality datasets from various galaxy imaging and spectroscopic surveys are available, such as Subaru Hyper Suprime-Cam (Miyazaki et al. 2012, 2015), Dark Energy Sur-

vey (The Dark Energy Survey Collaboration 2005), Kilo-Degree Survey (de Jong et al. 2015), Subaru Prime Focus Spectrograph (Takada et al. 2014), Dark Energy Spectroscopic Instrument (Levi et al. 2013), Large Synoptic Survey Telescope (Ivezic et al. 2008), Euclid (Laureijs et al. 2011), and WFIRST (Spergel et al. 2015).

Two-point statistics including galaxy-galaxy lensing can be studied in real and Fourier spaces. The power spectrum, defined as the square of the amplitude of the fluctuation as a function of scale in the Fourier space, is a fundamental statistics to study the physics in the evolution of cosmic density fluctuation. The power spectrum has been playing a central role in the analysis of cosmic microwave background (CMB) temperature/polarization fluctuation and galaxy clustering. One of the difficulties in measuring the Fourier-space statistics is the convolution of various observational effects including survey geometry and masks with the cosmological fluctuations in the Fourier space. In particular, weak lensing maps are affected by various observational issues such as complicated masks due to bright stars and their spikes, inhomogeneous noise due to signal-to-noise of imaging galaxies, and intrinsic noise

depending on the types of imaging galaxies. Due to the limited sky area and such complicated masks of imaging sky, the lensing analysis has been mainly conducted using the real-space statistics such as aperture-mass dispersion, two-point correlation functions for cosmic shear, and average  $\Delta\Sigma$  for galaxy-galaxy lensing. In partial sky, the information of the power spectrum is not identical to that of the two-point correlation due to the mask, which suggests that the complementary analysis using the power spectrum is important.

While real space approaches have been common for the cosmic shear analysis (e.g., Kilbinger et al. 2013; Heymans et al. 2013; Jee et al. 2013), Fourier space approaches are also of growing popularity in cosmic shear analysis. For instance, cosmic shear analysis using the pseudo-spectrum method, which has widely been used in CMB analysis (Hivon et al. 2002; Kogut et al. 2003; Brown et al. 2003; Bunn et al. 2003; Smith 2006; Smith & Zaldarriaga 2007; Grain et al. 2009; Kim & Naselsky 2010) including the extraction of B-mode polarization signals (Smith & Zaldarriaga 2007), has been proposed (Hikage et al. 2011; VanderPlas et al. 2012; Becker & Rozo 2016) and was applied to SDSS (Lin et al. 2012) and the Canada-France-Hawaii Telescope Lensing survey (CFHTLenS) data (Kitching et al. 2014). There is another method based on likelihood analysis to measure power spectrum estimation (Seljak 1998; Hu & White 2001), which was also applied to CFHTLenS data (Köhlinger et al. 2016). We note that recent cosmic shear analysis from the DES SV data presented results both in real and Fourier spaces (Becker et al. 2016).

In contrast, the galaxy-galaxy lensing analysis in the Fourier space has attracted little attention. This is presumably due to technical challenges mentioned above, but in fact the power spectrum analysis of galaxy-galaxy (or cluster-galaxy) lensing has several advantages. First, measuring signals from observations in the Fourier space are usually faster than that in the real space. This is particularly true when we are interested in large-scale cross lensing signals (the so-called two-halo component region) which contains important cosmological information (e.g., Hu & Jain 2004; Jeong et al. 2009; Oguri & Takada 2011; Covone et al. 2014; Sereno et al. 2015; Miyatake et al. 2016; Umetsu et al. 2015). Second, analytic calculations of signals and covariances in the Fourier space are easier than in the real space. Third, the covariance matrix is more diagonal in the Fourier space, and hence easier to handle.

In this paper, we extend the pseudo-spectrum method for cosmic shear developed in Hikage et al. (2011) to galaxy-galaxy lensing. The advantage of the pseudo-spectrum method is that the computational speed is much faster than the likelihood analysis, although the former approach requires careful corrections of the mask effect. We show that the pseudo-spectrum method works on the percent-level accuracy using ray-tracing simulations and halo datasets. We also study the covariance of galaxy-galaxy lensing power spectrum using the ray-tracing simulations to show that the so-called halo sample variance (HSV; Takada & Bridle 2007; Sato et al. 2009), and more generally speaking super sample covariance (SSC; Takada & Hu 2013; Li et al. 2014), plays an important role at small angular scales.

Furthermore, we apply the pseudo-spectrum method to publicly available observational datasets of CFHTLenS shape data (Heymans et al. 2012; Erben et al. 2013) to measure galaxy-galaxy lensing using various galaxy samples including Sloan Digital Sky Survey Luminous Red Galaxy (SDSS LRG; Eisenstein et al. 2001), and Baryonic Oscillation Spectroscopic Survey (BOSS) CMASS and LOWZ galaxy samples (Eisenstein et al. 2011). We evaluate the signal-to-noise ratio of our measurements and compare with

the model predictions using the analytically estimated covariance including Gaussian and HSV terms.

The paper is organized as follows. In Section 2 we present basic theoretical formulae of the galaxy-galaxy lensing spectrum. In Section 3, we present the formalism of pseudo-spectrum method applied to the lensing measurements. In Section 4, we apply the pseudo-spectrum method to simulated mock samples to test power spectrum reconstruction method. We also compare the covariance matrix between simulations and analytic formulae. In Section 5, we present the results on the pseudo-spectrum analysis applied to CFHTLenS and SDSS galaxy datasets. Section 6 is devoted to the conclusion.

## 2 FORMALISM

In this Section, we review the theoretical formalism of the shear power spectrum and galaxy-galaxy lensing spectrum (see the reviews of Bartelmann & Schneider 2001). Throughout the paper, the distance is expressed in comoving unit.

### 2.1 Galaxy-galaxy lensing spectrum

Weak lensing by the large-scale structure probes the convergence field  $\kappa$  that is defined by the projected mass density field  $\delta_m$  with the weight  $W^\kappa(z)$

$$\kappa(\theta) \equiv \int \frac{dz}{H(z)} W^\kappa(z) \delta_m(\theta; z), \quad (1)$$

where  $H(z)$  is the Hubble expansion rate at redshift  $z$  and the weight function  $W^\kappa(z)$  is defined as

$$W^\kappa(z) \equiv \bar{\rho}_m \Sigma_{\text{crit}}^{-1}(z), \quad (2)$$

with the mean matter density  $\bar{\rho}_m = \rho_{\text{crit}} \Omega_m$ . The inverse of the critical surface density  $\Sigma_{\text{crit}}^{-1}$  is given by

$$\Sigma_{\text{crit}}^{-1}(z) \equiv \int_z dz_s p(z_s) \Sigma_{\text{crit}}^{-1}(z, z_s), \quad (3)$$

$$\Sigma_{\text{crit}}^{-1}(z, z_s) = \frac{3H_0^2}{2\rho_{\text{crit}}} (1+z) \frac{d_A(z) d_A(z, z_s)}{d_A(z_s)}, \quad (4)$$

where  $d_A(z)$  is the comoving angular diameter distance at the redshift  $z$  and  $p(z_s)$  is the redshift distribution function of source galaxies normalized to be unity as  $\int dz_s p(z_s) = 1$ .

Galaxy-galaxy lensing, the cross-correlation between the number density field of foreground galaxies and the shear field of background galaxies, probes the relationship between matter and galaxy distribution as a function of scale. Using the Limber approximation (Limber 1954), the galaxy-galaxy spectrum is related to the three-dimensional (3D) galaxy-shear cross spectrum  $P^{gm}(k; z)$  as

$$\begin{aligned} C_\ell^{g\kappa} &\equiv \left\langle \tilde{\delta}_g \left( k = \frac{\ell}{d_A(z)} \right) \tilde{\kappa}_\ell^* \right\rangle, \\ &= \int_{z_{\min}}^{z_{\max}} \frac{dz}{H(z)} \left[ \frac{W^\kappa(z) W^g(z)}{d_A^2(z)} \right] P^{gm} \left( k = \frac{\ell}{d_A(z)}; z \right), \end{aligned} \quad (5)$$

where  $\tilde{\kappa}_\ell$  is the two-dimensional (2D) Fourier transform of  $\kappa(\theta)$  and  $\tilde{\delta}_g(k)$  is the Fourier transform of the projected number density fields of galaxies from  $z_{\min}$  to  $z_{\max}$ . The weight function  $W^g(z)$  is the redshift distribution of foreground galaxies normalized to be unity as  $\int_{z_{\min}}^{z_{\max}} dz W^g(z) = 1$ . Usually galaxy-galaxy lensing is measured in the real space using (differential) projected mass density around foreground galaxies  $\Delta\Sigma(R)$  as

$$\Delta\Sigma(R) \equiv \int \frac{kdk}{2\pi} P^{g\Sigma}(k) J_2(kR), \quad (6)$$

where  $J_2(x)$  is the second-order Bessel function. The cross spectrum of the projected mass density field  $\Sigma$  with the projected clustering of foreground galaxies  $P^{g\Sigma}(k)$  is related to the galaxy-matter power spectrum  $P^{gm}(k; z)$  as

$$P^{g\Sigma}(k) = \int_{z_{\min}}^{z_{\max}} \frac{dz}{H(z)} \bar{\rho}_m W^g(z) P^{gm}(k; z). \quad (7)$$

Note that the galaxy- $\Sigma$  cross spectrum  $P^{g\Sigma}(k)$  is independent of the source distribution. In the following analysis, we simply convert from  $C_\ell^{\kappa\kappa}$  to  $P^{g\Sigma}(k)$  at the mean redshift  $\bar{z}$  as

$$P^{g\Sigma}(k) \simeq d_A^2(\bar{z}) \Sigma_{\text{crit}}(\bar{z}) C_{\ell=k d_A(\bar{z})}^{g\kappa}, \quad (8)$$

where  $d_A^2(z)$  term comes from the conversion from multipole  $\ell$  to the wavenumber  $k$ .

## 2.2 Halo model approach to galaxy-galaxy lensing

In the halo model picture, the galaxy-shear cross spectrum is separated into one-halo and two-halo components

$$P^{g\Sigma} = P^{g\Sigma(1h)} + P^{g\Sigma(2h)}. \quad (9)$$

The one-halo term reflects the projected mass density profile within the host dark matter halo, and is given as

$$P^{g\Sigma(1h)}(k) = \int_{z_{\min}}^{z_{\max}} \frac{dz}{H(z)} \bar{\rho}_m W^g(z) \int dM \frac{dn}{dM} \frac{M}{\bar{\rho}_m} \times \tilde{u}_{\text{NFW}}(k; M, z) [\langle N_{\text{cen}} \rangle + \langle N_{\text{sat}} \rangle \tilde{p}_{\text{sat}}(k; M)], \quad (10)$$

where  $\tilde{u}_{\text{NFW}}$  is the Fourier transform of the projected NFW profile for the halo with mass  $M$  (Navarro et al. 1996; Wright & Brainerd 2000). In this paper, we employ the mass-concentration relation presented by Duffy et al. (2008).  $\langle N_{\text{cen}} \rangle$  and  $\langle N_{\text{sat}} \rangle$  represent the mean numbers of central and satellite galaxies, respectively, hosted by the halo with mass  $M$  based on the HOD formalism. The additional function  $p_{\text{sat}}$  represents the number density profile of satellite galaxies within the host halo which takes into account the off-centring of galaxies from the halo centre (Oguri & Takada 2011; Hikage et al. 2013). We use the Gaussian off-centring profile of satellites with the dispersion of the virial radius

$$\tilde{p}_{\text{sat}}(k; M) = \exp[-k^2 R_{\text{vir}}^2(M)/2]. \quad (11)$$

The two-halo term reflects the halo-matter clustering and given as

$$P^{g\Sigma(2h)}(k) = \int \frac{dz}{H(z)} \bar{\rho}_m W^g(z) \times \int dM \frac{dn}{dM} [\langle N_{\text{cen}} \rangle + \langle N_{\text{sat}} \rangle \tilde{p}_{\text{sat}}(k; M)] P_{\text{hm}}(k, z; M). \quad (12)$$

Here we simply describe the halo-matter power spectrum  $P_{\text{hm}}(k, z; M)$  as the linear matter power spectrum  $P_{\text{mm}}^{\text{lin}}(k, z)$  multiplied with the linear galaxy biasing  $b(M, z)$ . When comparing the observations, we use the fitting formula for both halo mass function  $dn/dM$  and bias  $b(M, z)$  (Tinker et al. 2008, 2010) where halo masses are defined as  $M_{200}$ , the mass enclosed in a sphere with an average density of 200 times the comoving matter density.

## 3 PSEUDO-SPECTRUM ANALYSIS

Here we present the formalism for the pseudo-spectrum analysis of galaxy-galaxy lensing by extending the pseudo-spectrum approach

of cosmic shear in Hikage et al. (2011). We use the flat-sky approximation for analyzing CFHTLenS data because the curvature effect is negligible compared to the sample variance and the computational cost is less expensive than the full-sky calculation. The full-sky formalism is presented in Appendix A. The shear field  $\gamma(\hat{\mathbf{n}})$  defined in a reference Cartesian coordinate system is decomposed into E-mode and B-mode components by the following Fourier transform

$$\tilde{E}_\ell \pm i\tilde{B}_\ell = \int d\hat{\mathbf{n}} \gamma(\hat{\mathbf{n}}) \exp(i\ell \cdot \hat{\mathbf{n}} \pm 2\varphi_\ell), \quad (13)$$

where  $\varphi_\ell$  is the azimuthal angle of  $\ell$ . Their auto and cross spectra are defined as

$$\langle X_\ell Y_{\ell'}^* \rangle \equiv (2\pi)^2 \delta_D^2(\ell - \ell') C_\ell^{XY}, \quad (14)$$

where  $X$  and  $Y$  denotes E- ( $\tilde{E}_\ell$ ) or B-mode ( $\tilde{B}_\ell$ ). In the weak lensing field, the E-mode field corresponds to the convergence field and thus its power spectrum reduces to the convergence power spectrum,  $C_\ell^{\kappa\kappa} = C_\ell^{EE}$ . In the standard  $\Lambda$  cold dark matter (CDM) model, the B-mode power and EB cross spectra are negligibly small and can be used to probe observational systematics. The galaxy-shear cross spectrum is also given by cross-correlating the projected galaxy distribution with the E-mode shear as

$$\left\langle \tilde{\delta}_g \left( \mathbf{k} = \frac{\ell}{d_A(z)} \right) \tilde{E}_{\ell'}^* \right\rangle \equiv (2\pi)^2 \delta_D^2(\ell - \ell') C_\ell^{gE}. \quad (15)$$

The cross-correlation of the galaxy distribution with the B-mode shear is also negligible and can be used to probe systematics.

An observed imaging field has a finite survey area with complicated masks. We take account of this mask effect using pseudo- $C_\ell$  method to reconstruct the original shear spectrum deconvolved with the survey mask. The weak lensing shear is usually estimated from observed ellipticities of background galaxy images. The galaxy ellipticity has a large intrinsic component and also the low signal-to-noise images are subject to the measurement noise

$$\mathbf{e}^{(\text{obs})}(\hat{\mathbf{n}}) = \gamma(\hat{\mathbf{n}}) + \epsilon_{\text{noi}}, \quad (16)$$

where  $\epsilon_{\text{noi}}$  includes the intrinsic ellipticity and the measurement noise. Ideally, the shear value is obtained by the average over observed ellipticities  $\gamma = \langle \mathbf{e}^{(\text{obs})} \rangle$ . However, the observed shear map is masked due to bright stars in our Galaxy and thus the survey mask has complicated shape due to bright stars and their spikes. When the grid is completely inside the mask, we do not obtain any information on the shear in the grid. Furthermore the expected error of shear in each grid depends on the number of source galaxies and the uncertainty of observed ellipticities, which can differ at different positions on the sky.

We thus estimate the weight for shear field by summing ellipticity weights in each pixel

$$U^\gamma(\hat{\mathbf{n}}) = \sum_i^{\hat{\mathbf{n}}_i \in \hat{\mathbf{n}}} w_i^\gamma, \quad (17)$$

where the shear weight of  $i$ -th source galaxy  $w_i^\gamma$  is introduced to enhance the signal-to-noise of weak lensing measurements. In practical analysis, it is common to define the weight of each galaxy by the inverse variance of the shape noise  $\epsilon_{\text{noi}}$ . The weight field takes account of the mask effect by setting the value of  $U^\gamma$  to be zero when the grid at  $\hat{\mathbf{n}}$  is completely masked. The observed shear field is related to the true shear field as

$$\langle \gamma^{(\text{obs})}(\hat{\mathbf{n}}) \rangle = \left\langle \sum_i^{\hat{\mathbf{n}}_i \in \hat{\mathbf{n}}} w_i^\gamma \mathbf{e}_i^{(\text{obs})} \right\rangle,$$

$$= U^\gamma(\hat{\mathbf{n}})\gamma^{(\text{true})}(\hat{\mathbf{n}}). \quad (18)$$

The weight field of  $\Sigma$  is similarly estimated by changing the weight  $w_i^\gamma$  to

$$w_i^\Sigma = [\Sigma_{\text{crit}}^{-1}(z; z_{s,i})]^2 w_i^\gamma. \quad (19)$$

The galaxy number density field is given by the excess of the observed galaxy number relative to the averaged number density at each grid. The observed galaxy distribution has different survey mask and angular selection function. For spectroscopic galaxy samples, there are more complicated observational effect such as the fiber collision that suppress the number of close pairs of galaxies. The observed field is related to the true field as

$$\langle \delta_g^{(\text{obs})}(\hat{\mathbf{n}}) \rangle = U^g(\hat{\mathbf{n}})\delta_g^{(\text{true})}(\hat{\mathbf{n}}), \quad (20)$$

where  $U^g$  is the weight (mask) field of the galaxy number density field. Here we focus on the small patch of the sky where the flat-sky approximation holds well. The Fourier transform of the shear field and the galaxy number density field are affected by the convolution of the masks

$$\tilde{E}_\ell^{(\text{obs})} \pm i\tilde{B}_\ell^{(\text{obs})} = \frac{1}{\theta_s^2} \sum_{\ell'} (\tilde{E}_{\ell'}^{(\text{true})} \pm i\tilde{B}_{\ell'}^{(\text{true})}) \tilde{U}_{\ell-\ell'}^\gamma e^{\pm 2i\varphi_{\ell'\ell}}, \quad (21)$$

where  $\varphi_{\ell'\ell} \equiv \varphi_{\ell'} - \varphi_\ell$  and

$$\tilde{\delta}_{g,\ell}^{(\text{obs})} = \frac{1}{\theta_s^2} \sum_{\ell'} \tilde{U}_{\ell-\ell'}^g \tilde{\delta}_{g,\ell'}^{(\text{true})}, \quad (22)$$

where we have assumed that the patch is a square field with the side length of  $\theta_s$ .

The auto and cross spectra in the sky field are defined as

$$\langle X_\ell Y_{\ell'}^* \rangle = \theta_s^2 \delta_{\ell-\ell'}^K C_\ell^{XY}, \quad (23)$$

where  $X$  and  $Y$  denote either E-mode shear, B-mode shear, or the galaxy number density field, and  $\delta_\ell^K$  is the Kronecker's delta. Again we do not take into account the imaginary part of cross spectra. Due to the convolution with the mask (weight) field in the real space, the power spectrum for the mask (weight) field has the mode coupling as

$$\mathbf{C}_\ell^{(\text{obs})} = \sum_{\ell'} \mathbf{M}_{\ell\ell'} F_{\ell'}^2 C_{\ell'}^{(\text{true})} + \mathbf{N}_\ell^{(\text{obs})}, \quad (24)$$

where we introduce the 6-dimensional vector  $\mathbf{C}_\ell = (C_\ell^{EE}, C_\ell^{BB}, C_\ell^{EB}, C_\ell^{BE}, C_\ell^{gE}, C_\ell^{gB}, C_\ell^{gg})$ ,  $\mathbf{M}$  is  $6 \times 6$  convolution matrix,  $F_\ell$  is the pixel window function and  $\mathbf{N}_\ell^{(\text{obs})}$  is the convolved noise spectrum. For the lensing power spectrum, the E-mode and B-mode power spectra are mixed as

$$\begin{pmatrix} \tilde{C}_\ell^{\text{EE}(\text{obs})} \\ \tilde{C}_\ell^{\text{BB}(\text{obs})} \end{pmatrix} = \frac{1}{\theta_s^2} \sum_{\ell'} \mathcal{U}_{\ell-\ell'}^{\gamma\gamma} \begin{pmatrix} \cos^2(2\varphi_{\ell\ell'}) & \sin^2(2\varphi_{\ell\ell'}) \\ \sin^2(2\varphi_{\ell\ell'}) & \cos^2(2\varphi_{\ell\ell'}) \end{pmatrix} \times \begin{pmatrix} C_\ell^{\text{EE}(\text{true})} \\ C_\ell^{\text{BB}(\text{true})} \end{pmatrix}. \quad (25)$$

The convolution with the mask generates the B-mode spectrum leaked from the E-mode spectrum even if there is no intrinsic B-mode power. On the other hand, galaxy-shear cross spectra are written as

$$C_\ell^{gX(\text{obs})} = \frac{1}{\theta_s^2} \sum_{\ell'} C_{\ell'}^{gX(\text{true})} \mathcal{U}_{\ell-\ell'}^{g\gamma} \cos(2\varphi_{\ell\ell'}), \quad (26)$$

where  $X$  denotes E- or B-mode shear field. E-mode and B-mode components do not mix for the galaxy-shear cross spectra because

of their different parity. The EB-mode cross spectrum and the galaxy auto power spectrum are respectively written as

$$C_\ell^{\text{EB}(\text{obs})} = \frac{1}{\theta_s^2} \sum_{\ell'} C_{\ell'}^{\text{EB}(\text{true})} \mathcal{U}_{\ell-\ell'}^{\gamma\gamma} [\cos^2(2\varphi_{\ell\ell'}) - \sin^2(2\varphi_{\ell\ell'})], \quad (27)$$

and

$$C_\ell^{gg(\text{obs})} = \frac{1}{\theta_s^2} \sum_{\ell'} C_{\ell'}^{gg(\text{true})} \mathcal{U}_{\ell-\ell'}^{gg}. \quad (28)$$

In the above expressions, the function  $\mathcal{U}_\ell$  represent the auto and cross power spectra of shear and galaxy weight fields, i.e.,

$$\langle \tilde{U}_{X,\ell} \tilde{U}_{Y,\ell'}^* \rangle = \theta_s^2 \delta_{\ell-\ell'}^K \mathcal{U}_\ell^{XY}, \quad (29)$$

with  $X$  and  $Y$  being  $g$  or  $\gamma$ . Note that the two weight field  $U^\gamma(\hat{\mathbf{n}})$  and  $U^g(\hat{\mathbf{n}})$  are not necessarily identical; our formalism works even if the shear and galaxy density fields have different mask patterns. We also take account of the effect of the finite square field to compute the full mode coupling matrix  $M_{\ell\ell'}$  (Hikage et al. 2011).

We invert the mode coupling matrix after binning. To do so, we compute the binned non-dimensional power spectrum as

$$C_b \equiv \frac{1}{N_{\text{mode},b}} \sum_{\ell}^{\ell \in \ell_b} P_{b\ell} C_\ell, \quad (30)$$

where  $P_{b\ell} = \ell^2/2\pi$  and  $N_{\text{mode},b}$  is the number of modes in  $b$ -th bin. The unmasked binned power spectrum is obtained by multiplying the inverse of the mode coupling matrix with the pseudo-spectrum

$$C_b^{(\text{true})} = \mathbf{M}_{bb'}^{-1} \sum_{\ell}^{\ell \in \ell'_b} P_{b'\ell} (\mathbf{C}_\ell^{(\text{obs})} - \langle \mathbf{N}_\ell \rangle_{\text{MC}}), \quad (31)$$

where

$$\mathbf{M}_{bb'} = \sum_{\ell}^{\ell \in \ell_b} \sum_{\ell'}^{\ell' \in \ell'_b} P_{b\ell} \mathbf{M}_{\ell\ell'} F_{\ell'}^2 Q_{\ell'b'}, \quad (32)$$

with  $Q_{\ell b} = 2\pi/\ell^2$ . In order to remove the shot noise effect, we randomly rotate ellipticities of individual weak lensing galaxies to estimate the shot noise power spectrum  $\langle \mathbf{N}_\ell \rangle_{\text{MC}}$  and to subtract it from the power spectrum. In order to obtain accurate estimates of the shot noise power spectrum, we generate 100 realizations of rotated shear fields and take their average of  $\tilde{\mathbf{N}}_\ell$ . Throughout the paper we use 15  $\ell$  bins in the range  $100 \leq \ell \leq 10800$  that are equal spaced in the logarithmic scale.

## 4 TESTING THE PSEUDO-SPECTRUM METHOD USING RAY-TRACING SIMULATIONS

### 4.1 Ray-tracing simulations and halo samples

Ray-tracing simulations in  $N$ -body simulations have been used to study the properties of weak lensing fields (e.g., Jain et al. 2000; Hamana & Mellier 2001). We use ray-tracing simulations and the halo dataset constructed by Sato et al. (2009) to check the accuracy of our pseudo-spectrum method. We use 400 realizations of shear field which has the square field with a side length  $\theta_s = 5$  degree and the pixel number of  $N_{\text{pix}} = 2048^2$ . The redshift of the source galaxy is set to  $z_s = 1$ . At  $z < 1$ , the mass field is obtained from  $N$ -body simulations with  $L_{\text{box}} = 240h^{-1}\text{Mpc}$  and  $256^3$  particles (each particle mass is  $5.44 \times 10^{10} h^{-1} M_\odot$ ) at the initial redshift



of 50. Cosmological parameters in these simulations are those in the flat  $\Lambda$  CDM model based on the *WMAP* 3-year result (Spergel et al. 2007):  $\Omega_m = 0.238$ ,  $\Omega_b = 0.042$ ,  $\Omega_\Lambda = 0.762$ ,  $\sigma_8 = 0.76$ ,  $h = 0.732$ ,  $n_s = 0.958$  (hereafter we denote *WMAP3*).

The simulated source galaxies are distributed randomly with the mean angular number density of  $n_{s,\text{gal}} = 20 \text{ arcmin}^{-2}$ . Each source galaxy takes the shear value at the nearest pixel point in a given shear field. We add an intrinsic shape noise to each ellipticity component assuming a Gaussian distribution with the dispersion per component of  $\sigma_{\text{int}} = 0.22$ . We take into account the mask due to bright stars and their diffraction spikes as described in Hikage et al. (2011). The radii of the simulated star mask  $r$  randomly distributes from 0.2 to 2 arcmin. For each star mask with  $r > 1$  arcmin, a rectangular shape mask with  $0.2r \times 5r$  along  $y$ -axis is added to mimic the diffraction spike. We remove source galaxies inside the masks so that 75% of the total area is available after masking. The shear field with the inverse variance weight becomes

$$\gamma'(\mathbf{x}) = \sum_{i \in \mathbf{x}} w_i (\gamma_i + \epsilon_{\text{int}}), \quad (33)$$

and the shear weight field is  $U^\gamma(\mathbf{x}) = \sum_{i \in \mathbf{x}} w_i$ . For simplicity we set the noise variance for all the simulated source galaxies to be same (i.e.,  $w_i = \text{const}$ ) and thus the shear weight is simply proportional to the source number density. Even when  $w_i$  is constant, the shear weight field is fluctuated depending on the number distribution of source galaxies. When a pixel  $\mathbf{x}$  is partially (completely) masked, the relative weight for the pixel becomes less than unity (zero).

The ray-tracing simulations also contain haloes identified from the  $N$ -body simulations used for ray-tracing. We use the haloes with the mass  $M_h \geq 10^{13} h^{-1} M_\odot$  and  $M_h \geq 10^{14} h^{-1} M_\odot$  at the redshift range of  $0.4 < z < 0.6$  as a foreground lens sample. The masked density fluctuation of these foreground “galaxies” is obtained by using the data and random as follows:

$$\delta'_g(\mathbf{x}) = n_g(\mathbf{x}) - \bar{n}(\mathbf{x}), \quad (34)$$

where  $\bar{n}(\mathbf{x})$  is the mean number density estimated from random and the resulting weight field for the galaxies  $U^g(\mathbf{x}) = \bar{n}(\mathbf{x})$ . The sky areas covered by imaging surveys and spectroscopic surveys are usually different. We mask different 25% areas in the simulated halo fields and the source fields. The overlapped area reduces to be 50% of the original area.

## 4.2 Reconstruction of the input spectra

Fig. 1 shows the results of simulated galaxy (halo)-shear cross spectra  $P^{g\Sigma}(k)$ , which is essentially the galaxy-galaxy lensing profile in the Fourier space. The errorbars represent the  $1\sigma$  error for the averaged spectra obtained by computing the dispersion of the spectra reconstructed using the pseudo-spectrum method divided by the square root of the realization number, 400. We confirm that the deconvolved spectra (red symbols) recover the input galaxy-shear cross spectra (black solid lines) for both cases with the halo mass  $M_h > 10^{13} M h_\odot^{-1}$  and  $M_h > 10^{14} M h_\odot^{-1}$ . The masked spectra (blue symbols) have different amplitudes and shapes. As shown in the middle panels of Fig. 1, the difference ratios of the deconvolved spectra to the input spectra are within the errors for a wide range from 0.1 to  $10h/\text{Mpc}$  scale. The bottom panels show the cross-spectra between the halo density fields and the B-mode lensing fields, which are also consistent with zero. This analysis clearly indicates that our pseudo-spectrum method accurately recovers the

input galaxy-shear cross spectrum, even in the presence of realistic masks.

## 4.3 Covariance of galaxy-galaxy lensing

Our extensive galaxy-shear cross-spectrum analysis using ray-tracing simulations also enables us to quantify the covariance of galaxy-galaxy lensing. Although the weak lensed field is non-Gaussian (e.g., Takada & Jain 2009; Kayo et al. 2013; Sato & Nishimichi 2013), observed weak lensed fields are dominated by the shape noise on small scales, and thereby the Gaussian approximation has often been adopted. In Gaussian approximation, the covariance matrix of galaxy-shear cross spectrum is diagonal and is described by

$$\text{Cov}_{g\Sigma}^{(G)}(k_i, k_j) = \frac{\delta_{ij}^K}{N_{\text{mode},i}} [P^{g\Sigma 2}(k_i) + \tilde{P}^{gg}(k_i) \tilde{P}^{\Sigma\Sigma}(k_i)], \quad (35)$$

where the power spectrum  $\tilde{P}$  denotes the power spectrum including shot noise. At small scales, this covariance matrix is dominated by the shot noise term  $\propto \sigma_{\text{int}}^2 / (n_{s,\text{gal}} \bar{n}_g)$ , where  $\bar{n}_g$  is the average density of foreground galaxies (see, e.g., Oguri & Takada 2011). The number of independent  $k$ -modes in  $i$ -th bin,  $N_{\text{mode},i}$ , is given as

$$N_{\text{mode},i} = \frac{\pi(k_{i,\text{max}}^2 - k_{i,\text{min}}^2) \Omega_{\text{sky}}^{\text{overlap}}}{(2\pi)^2}, \quad (36)$$

where  $\Omega_{\text{sky}}^{\text{overlap}}$  is the overlapped sky area between halo maps and shear maps.

Fig. 2 compares the errors of diagonal components for galaxy-shear cross spectrum relative to the Gaussian expectations. The Gaussian errors for simulations is computed using the simulated spectrum. On large scales (small  $\ell$ ), the relative errors are close to be unity, indicating that the Gaussian approximation is reasonable. On larger  $\ell$ , however, the relative errors increase and have peak at  $k \sim 3 - 5h/\text{Mpc}$  depending on the halo mass.

We find that this excess of the covariance at small scales can be explained by the halo sample variance (HSV). In the finite survey area, mode fluctuations whose scales are larger than the survey area are known to generate the excess covariance in the lensing auto power spectra (Takada & Bridle 2007; Sato et al. 2009). The more complete formulae called super sample covariance (SSC), which include the beat coupling (BC) and the cross-term BC-HSV, was formulated in Takada & Hu (2013) and Li et al. (2014). For the shear auto power spectrum and galaxy-shear cross spectrum, HSV contributions to the covariances are written as (Takada & Hu 2013)

$$\text{Cov}_{\kappa\kappa}^{(\text{HSV})} = \int \frac{dz}{H(z)} \frac{W^{\kappa 4}(z)}{d_A^6(z)} I_{\text{mm}}(k_i, k_i) I_{\text{mm}}(k_j, k_j) (\sigma_W^L(z))^2, \quad (37)$$

and

$$\text{Cov}_{g\Sigma}^{(\text{HSV})} = \int_{z_{\text{min}}}^{z_{\text{max}}} \frac{dz}{H(z)} [W^g(z) W^\Sigma(z)]^2 \frac{1}{d_A^6(z)} \times I_{gm}(k_i, k_i) I_{gm}(k_j, k_j) (\sigma_W^L(z))^2, \quad (38)$$

where  $W^\Sigma(z) = \Sigma_{\text{crit}}(z) W^\kappa$  and

$$I_{\text{mm}}(k, k') \equiv \int dM \frac{dn}{dM} \left( \frac{M}{\bar{\rho}_m} \right)^2 b(M, z) \tilde{u}_{\text{NFW}}^2(k; M, z), \quad (39)$$

and

$$I_{gm}(k, k') \equiv \frac{1}{\bar{n}_g} \int dM \frac{dn}{dM} \left( \frac{M}{\bar{\rho}_m} \right) (b(M, z) - 1) \tilde{u}_{\text{NFW}}(k; M, z)$$

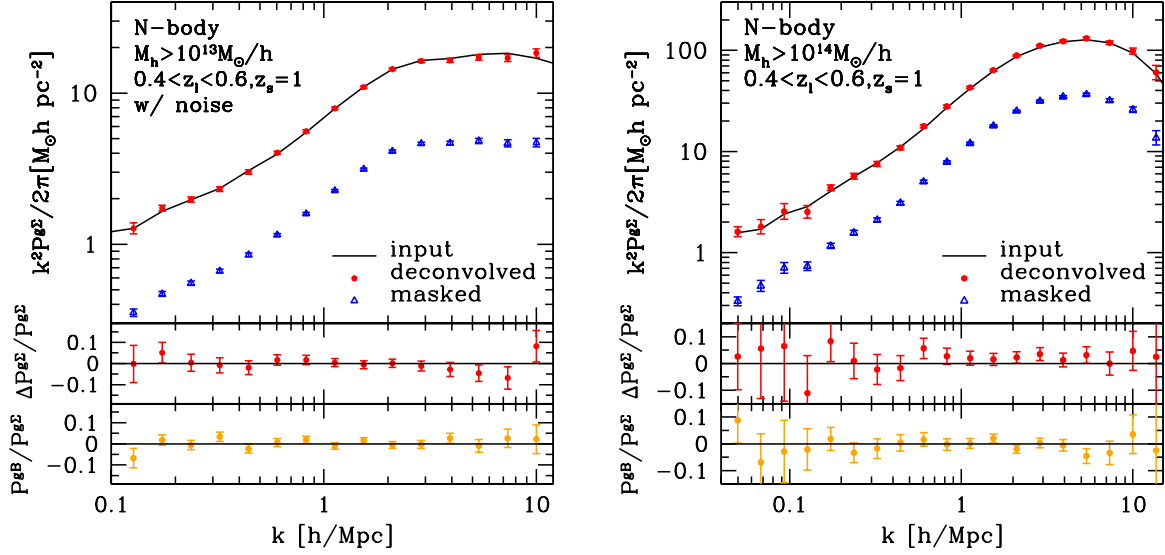


**Figure 1.** Reconstruction of the galaxy-shear cross spectrum  $P_{g\Sigma}(k)$ , i.e., cross-correlation of the weak lensing shear field and the halo number density field, using 400 realizations of ray-tracing simulations and halo catalogues. Each realization covers  $25 \text{ deg}^2$ . The mask regions are different between the shear and halo number density fields, and the fraction of overlapping area is 50% (see text for details). The source redshift is  $z_s = 1$  and the angular number density of source galaxies for weak lensing is  $20 \text{ arcmin}^{-2}$ . The intrinsic shape noise is Gaussian with  $\sigma_{\text{int}} = 0.22$ . We use haloes with minimum halo masses of  $10^{13} h^{-1} M_\odot$  (left) and  $10^{14} h^{-1} M_\odot$  (right). *Top:* The input cross spectra are plotted by solid lines. The deconvolved spectra and masked spectra are respectively plotted by red filled circles and blue open triangles. *Middle:* The difference ratio between the deconvolved spectrum and the input spectrum. *Bottom:* The cross-correlation between halo density fields and the lensing B-mode field.

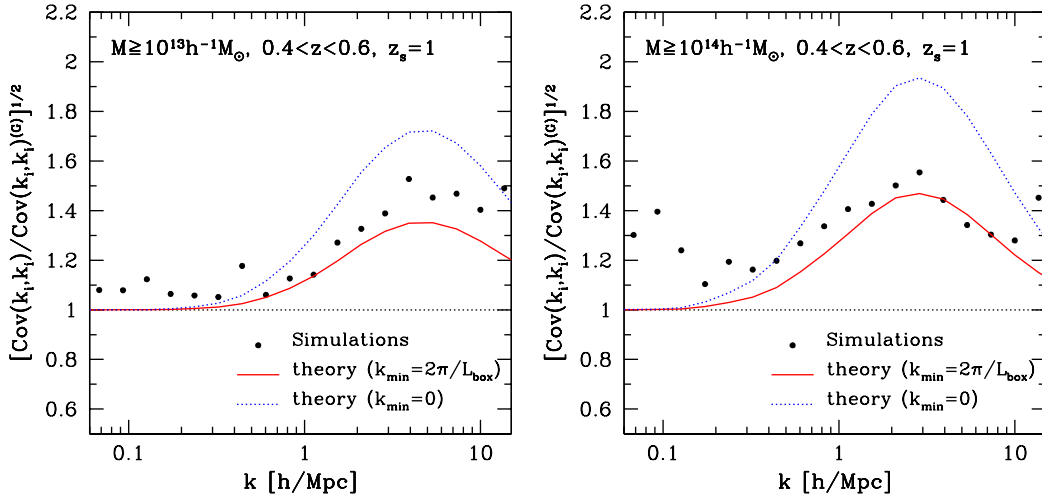


**Figure 2.** Diagonal errors of the simulated deconvolved galaxy-shear cross spectra relative to the Gaussian errors (eq. [35]). Left and right panels show the results for the halo masses of  $10^{13} h^{-1} M_\odot$  and  $10^{14} h^{-1} M_\odot$ , respectively. Lines represent the theoretical expectations from the HSV including fluctuations up to the simulation box size (solid) and including fluctuations at all scales (dotted).

$$\left[ \langle N_{\text{cen}} \rangle + \langle N_{\text{sat}} \rangle \tilde{p}_{\text{sat}}(k'; M, z) \right] \cdot (40)$$

For the galaxy-shear cross power spectrum, we use  $b(M) - 1$  instead of  $b(M)$ , which comes from local averaging of galaxy number counts as discussed in the section II C in Takada & Hu (2013). Since the local averaging rescales the observed power as  $P_W(k) = P(k)/(1 + \delta_b)$ , the HSV effect is reduced to some ex-

periment. The response of the galaxy-galaxy lensing to the background is modified as

$$\frac{\partial P(k)}{\partial \delta_b} \rightarrow \frac{\partial P(k)}{\partial \delta_b} - P(k), \quad (41)$$

which corresponds to converting  $b(M)$  to  $b(M) - 1$ .

The variance  $(\sigma_W^L)^2$  represents the amplitude of the background fluctuation in a given survey window

$$(\sigma_W^L(z))^2 = \frac{1}{\Omega_{\text{sky}}^2} \int_{k_{\min}} \frac{d\mathbf{k}}{(2\pi)^2} |\tilde{W}(\mathbf{k})|^2 P^L \left( k = \frac{\ell}{d_A(z)}; z \right), \quad (42)$$

where  $P^L(k; z)$  is the 3D linear power spectrum at  $z$  and  $k_{\min}$  denotes the minimum wavenumber. The variance of the background fluctuations  $(\sigma_W^L)^2$  increases as the survey area decreases. The ray-tracing simulations used in this paper are constructed from  $N$ -body simulation boxes with the side length of  $L_{\text{box}} = 240h^{-1}\text{Mpc}$  up to  $z = 1$ . In comparisons with the simulation results, we set  $k_{\min} = 2\pi/L_{\text{box}}$  with  $L_{\text{box}} = 240h^{-1}\text{Mpc}$  so that the fluctuations at scales larger than  $L_{\text{box}}$  are excluded. As a result,  $(\sigma_W^L)^2$  is decreased roughly by half. When the field has a square shape, the survey window function reads

$$\tilde{W}(\mathbf{k}) = L^2 \text{sinc}(k_x L/2) \text{sinc}(k_y L/2), \quad (43)$$

where  $L$  is a side length of the square field. In this paper, we approximate the square-shape survey window function with  $L = (\Omega_{\text{sky}}^{\text{overlap}})^{1/2}$ .

In Fig. 2, we compare the ratio of the diagonal elements of the covariance matrix from our simulations to the Gaussian covariance with theoretical expectations of the enhancement of the covariance matrix due to the HSV effect. Since we use dark haloes to represent galaxies, in computing the HSV contributions the HOD parameters are set to  $\langle N_{\text{sat}} \rangle = 0$  for all  $M_h$  and  $\langle N_{\text{cen}} \rangle = 1$  for  $M_h \geq 10^{13}h^{-1}M_\odot$  or  $10^{14}h^{-1}M_\odot$  and  $\langle N_{\text{cen}} \rangle = 0$  otherwise. We find that the simulations and HSV expectations agree reasonably well with each other, particularly when  $k_{\min}$  is set to the simulation box size. The HSV contribution is comparable to the Gaussian term on large  $l$  and thus the total variance increases by 30-40%. When the background fluctuation larger than box size is included, which is relevant for the covariance in real observations, the HSV contribution surpasses the Gaussian one and the total variance doubles.

More importantly, the HSV induces off-diagonal elements in the covariance matrix, as shown in equation (38). We compute the correlation coefficient matrix of the galaxy-shear cross spectrum as

$$R_{ij} = \frac{\text{Cov}_{g\Sigma}(k_i, k_j)}{\sqrt{\text{Cov}_{g\Sigma}(k_i, k_i) \text{Cov}_{g\Sigma}(k_j, k_j)}}. \quad (44)$$

Upper panels of Fig. 3 show our simulation results on the covariance matrix for the galaxy-shear cross spectrum with the halo mass  $M_h \geq 10^{13}h^{-1}M_\odot$ . When the shape noise is not included (left panel), the mode coupling due to the nonlinear gravity increases the covariance among different scales at larger  $k$ . When the shape noise is included (right panel), the covariance matrix approaches to be Gaussian. However, there are still residuals in the off-diagonal components at small scales. We find that the residual covariance is consistent with the predictions of Gaussian plus the HSV term, as shown in the lower panels of Fig. 3. This analysis suggests that the covariance matrix computed by adding the Gaussian covariance and the HSV contribution provides a good approximation to the covariance from our simulations which include full non-Gaussian effects. We note that Gruen et al. (2015) argued that intrinsic variations of the projected density profiles serve as a source of off-diagonal covariance matrix at small scales. Our analysis implies that the effect of the intrinsic variations is small compared with the HSV contribution, at least in our setting where the halo mass range is rather broad. In what follows, we use the analytic formulae of the covariance  $\text{Cov}^{(G)} + \text{Cov}^{\text{HSV}}$ . In the following analysis, we show how the difference in the results with and without the HSV contribution.

## 5 APPLICATIONS TO CFHTLEN S DATA AND BOSS GALAXY DATASET

### 5.1 CFHTLenS data

Here we use public available Canada-France-Hawaii Telescope Lensing Survey (CFHTLenS) catalogue (Erben et al. 2013). CFHTLenS data consists of 171 pointings (field of view of each pointing is  $\sim 1 \text{ deg}^2$ ) in 4 disjoint fields (W1, W2, W3, W4) covering an total effective survey area of  $154 \text{ deg}^2$ . The imaging survey is carried out using 300 mega pixels MEGACAM instrument with five filters and the  $i$ -band magnitude limit  $i_{AB} < 24.5$  ( $5\sigma$  in a  $2''$  aperture).

We use the imaging data classified as a galaxy (*fitclass*=0) and unmasked object (*MASK*  $\leq 1$ ). The galaxy shape is measured based on the *lensfit* algorithm (Miller et al. 2013) and the ellipticity is defined as  $e = (a - b)/(a + b)$  ( $a$  and  $b$  are major and minor axes). The ellipticity data is obtained as a two-dimensional vector  $(e_1, e_2)$  where  $e_1$  is the ellipticity component along the constant declination and  $e_2$  axis. Following the shear calibration by Heymans et al. (2012), the additive term  $c_2$  is subtracted from the measured  $e_2$ . Furthermore, each ellipticity component is divided by the multiplicative term  $m$  calibrated using simulations as a function of image S/N and galaxy size (Miller et al. 2013). The averaged values of the galaxy shape ellipticity is 0.22 per component. We use the ellipticity data with a positive value of the weight, which is determined by the inverse of the variance due to the intrinsic galaxy ellipticity and shape measurement error due to photon noise (Miller et al. 2013).

Since the galaxy-galaxy lensing measurement is much less affected by the systematics than cosmic shear analysis, we use the data in the whole of CFHTLenS fields. The photometric redshift of each galaxy is estimated by the Bayesian Photometric Redshift (BPZ) code (Benítez 2000; Hildebrandt et al. 2012). We use source galaxies with photo- $z$  up to  $z_{\text{BPZ}} = 3.1$  but the probability  $P_{\text{BPZ}}(z > z_{\text{max}}) \geq 0.84$  where  $z_{\text{max}}$  is the maximum redshift of a given spectroscopic sample used as a foreground lens sample for the galaxy-shear cross spectrum analysis (see also Oguri 2014, for a similar background galaxy selection). The angular number density of source galaxies becomes  $n_s = 7.2 \text{ arcmin}^{-2}$  for CMASS and  $9.6 \text{ arcmin}^{-2}$  for LOWZ.

We set a square field with a side length of 600 arcmin to cover each CFHTLenS field. The centre of the square field is defined as  $\alpha_c = (\alpha_{\text{max}} + \alpha_{\text{min}})/2$  and  $\delta_c = (\delta_{\text{max}} + \delta_{\text{min}})/2$  where  $\alpha_{\text{max}(\text{min})}$  and  $\delta_{\text{max}(\text{min})}$  is the maximum (minimum) value of right ascension and declination of source galaxies in each CFHTLenS field. We convert the spherical coordinates to flat coordinates as  $\cos(x) = \sin^2(\delta) + \cos^2(\delta) \cos(\alpha - \alpha_c)$  and  $y = \delta - \delta_c$  (Kilbinger et al. 2013).

### 5.2 Spectroscopic samples

In order to cross-correlate with the CFHTLenS shear data, we use a public catalogue of SDSS-III Data Release 11 BOSS spectroscopic galaxies and the random catalogues (Eisenstein et al. 2011). We use two main BOSS galaxy samples, “LOWZ” (lower redshift sample at  $z < 0.4$ ) and “CMASS” (higher redshift sample at  $0.4 < z < 0.7$ ) (see the details of the sample selection in Eisenstein et al. 2011; Ahn et al. 2012; Dawson et al. 2013). We focus on the redshift range of  $0.16 < z < 0.33$  for LOWZ and  $0.47 < z < 0.59$  for CMASS where the sample is nearly volume-limited with a constant number density. We also use a classical

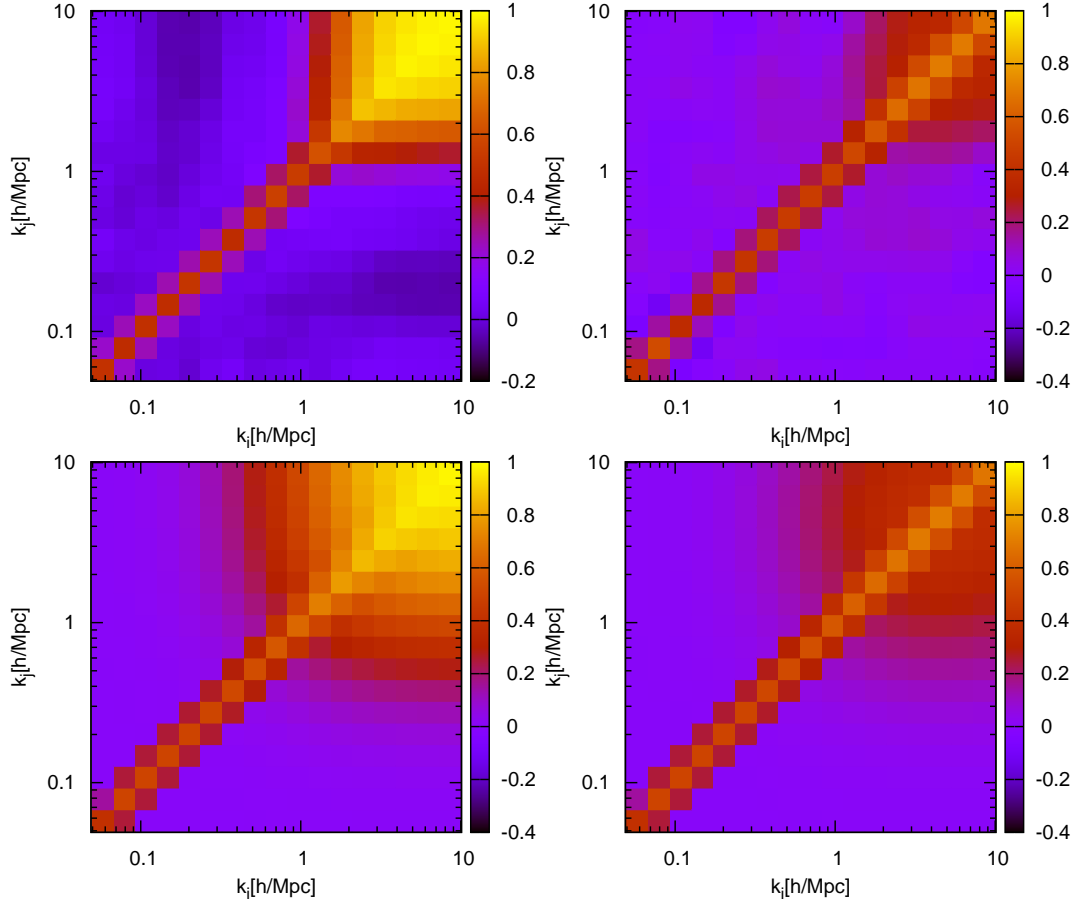


**Figure 3.** Correlation coefficient matrix (eq. [44]) of the galaxy-shear cross spectrum  $P^{g\Sigma}(k)$  for  $M_h \geq 10^{13} h^{-1} M_\odot$  with (right panels) and without shape noise (left panels). Upper panels show the correlation coefficient matrix derived from the simulated deconvolved galaxy-shear cross spectrum. Lower panels show the theoretical prediction of the covariance including the Gaussian covariance and the HSV contribution.

SDSS-I Luminous Red Galaxies (LRGs) (Eisenstein et al. 2001). Targeting cuts of the LRGs are similar to the BOSS LOWZ and CMASS galaxies, though BOSS sample contains lower stellar mass galaxies and their number density is about three times higher than LRGs.

These spectroscopic samples partially overlap with the CFHTLenS fields. The overlapped galaxy number becomes 418 for SDSS/LRG ( $0.16 < z < 0.33$ ), 2353 for BOSS/LOWZ ( $0.16 < z < 0.33$ ), and 5429 for BOSS/CMASS ( $0.47 < z < 0.59$ ) samples. The overlapped sky fraction of CFHTLenS field is 35 % for LRG, 74% for LOWZ and 77% for CMASS sample. There is almost no overlap for the field W2 and thus we do not use W2 field in our galaxy-galaxy lensing analysis.

### 5.3 Results

We measure the galaxy-shear cross spectrum  $P^{g\Sigma}(k)$ , i.e., the galaxy-galaxy lensing profile in the Fourier space, using the pseudo-spectrum method. Fig. 4 show the comparison of measured cross spectra between the CFHTLenS shear catalogue and three spectroscopic samples: BOSS/CMASS ( $0.47 < z < 0.59$ ), BOSS/LOWZ ( $0.16 < z < 0.33$ ), and SDSS DR7 LRG ( $0.16 < z < 0.33$ ). When converting from  $C_\ell^{g\kappa}$  to  $P^{g\Sigma}$ , for simplicity we use the mean redshift  $\bar{z}$  of each galaxy sample assuming a flat  $\Lambda$ CDM cosmology with  $\Omega_m = 0.3$  (eq. [8]). We find that the

cross-correlation with the SDSS LRG sample has larger amplitude at larger  $k$ . This is consistent with that the SDSS/LRGs are hosted by more massive haloes than the other two samples (see also Miyatake et al. 2015).

We estimate the signal-to-noise ratio for the galaxy-shear cross spectrum as

$$(S/N)^2 = \sum_{i,j} P^{g\Sigma}(k_i) (\text{Cov}^{g\Sigma})^{-1}_{ij} P^{g\Sigma}(k_j). \quad (45)$$

We use the range of scales from  $0.1 h^{-1} \text{Mpc}$  to  $10 h^{-1} \text{Mpc}$  with 15 data points. Here the covariance is estimated analytically using the Gaussian covariance and the HSV contribution (see Section 4.3). The S/N of the galaxy-galaxy lensing for the three galaxy samples are 7.1 (SDSS/LRG), 8.6 (BOSS/LOWZ), and 10.4 (BOSS/CMASS). For comparison, the S/N increases to 18.1 (SDSS/LRG), 23.7 (BOSS/LOWZ), 20.4 (BOSS/CMASS) without the HSV term in the covariance. The S/N value decreases nearly by half when including the HSV, which indicate that the effect of super survey modes is important also for the galaxy-galaxy lensing analysis. Even when the HSV is taken into account, we find that galaxy-galaxy lensing signals are detected at the significance level of  $7 - 10\sigma$  for all of the three spectroscopic samples.

We compare the measured spectra with the halo model calculations assuming a commonly used HOD form with 5 parameters



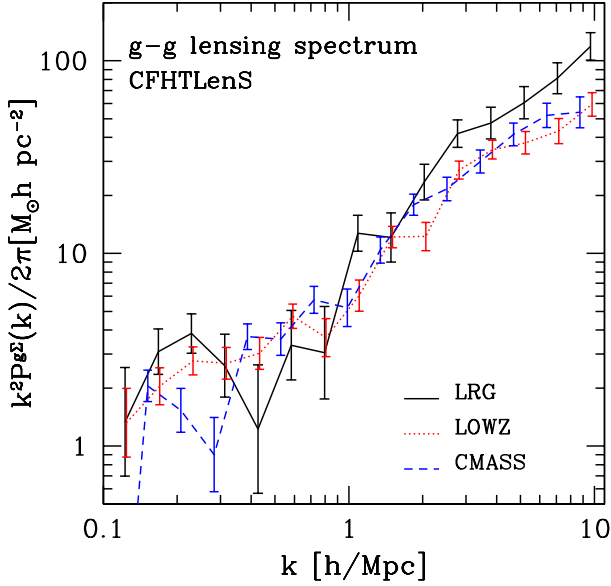


**Figure 4.** The galaxy-galaxy lensing pseudo spectrum, i.e., the galaxy-shear cross spectrum with the correction of the masking effect, between the CFHTLenS shear catalogue and three different spectroscopic galaxy samples, SDSS DR7 LRG (solid), BOSS/LOWZ (dotted), and BOSS/CMASS (dashed).

by Zheng et al. (2005)

$$\begin{aligned} \langle N_{\text{cen}} \rangle &= \frac{1}{2} \left[ 1 + \text{erf} \left( \frac{\log_{10}(M) - \log_{10}(M_c)}{\sigma_{\log M}} \right) \right], \\ \langle N_{\text{sat}} \rangle &= \langle N_{\text{cen}} \rangle \left( \frac{M - M_0}{M_1} \right)^\alpha, \end{aligned} \quad (46)$$

where  $\text{erf}(x)$  is the error function and their HOD parameters in the previous work are listed in Table 1. The HOD parameter values for LRGs (Reid & Spergel 2009) is estimated using the counts-in-cylinder group finding technique based on *WMAP3* cosmology, while the others are estimated from redshift-space clustering based on *WMAP7* cosmology (Manera et al. 2013, 2015). When comparing the HOD model predictions with our measurements, we use the same cosmological parameters as those assumed when deriving the HOD parameter values. The difference of the cosmology is included in the conversion from  $C_\ell^{g\kappa}$  to  $P^{g\Sigma}(k)$  as  $P^{g\Sigma}(k) \rightarrow P^{g\Sigma}(k)[d_A^2 \Sigma_{\text{crit}}^{(\text{fid})}]/[d_A^2 \Sigma_{\text{crit}}]$  and  $k \rightarrow kd_A(z)/d_A^{(\text{fid})}(z)$ , though the conversion effect is much smaller than the statistical error.

Fig. 5 compares the HOD model predictions with observed spectra. Individual contributions from the one-halo and two-halo components are plotted separately. We find that the halo model with the HOD parameters in previous work well explains our measured galaxy-shear cross spectra. To quantify the goodness, we estimate the  $\chi^2$  value as

$$\chi^2 = \sum_{i,j} \Delta P^{g\Sigma}(k_i) (\text{Cov}^{g\Sigma})^{-1}_{ij} \Delta P^{g\Sigma}(k_j), \quad (47)$$

where  $\Delta P^{g\Sigma}(k)$  is defined by the difference between the observed spectrum and the model spectrum. For all of the three spectroscopic galaxy samples, we obtain reasonable  $\chi^2$  values as listed in Table 1. The consistency of the HOD between the different measurements indicates that the halo model description works well in the

current uncertainty level. This consistency can also serve as a sanity check that our pseudo-spectrum method works well with real observational data. The right panels in Fig. 5 show that the comparison of galaxy-shear cross spectra for three CFHTLenS fields (W1, W3, W4). We find that the galaxy-shear cross spectra are detected in each field and they are consistent with each other.

## 6 CONCLUSION

In this paper, we have presented the formalism of galaxy-galaxy lensing in the Fourier space. Our approach takes account of the realistic mask effect using the pseudo-spectrum method. Using ray-tracing simulations in  $N$ -body simulations, we have confirmed that the pseudo-spectrum method successfully recovers the input true galaxy-shear cross spectrum, which is a Fourier space counterpart of the stacked galaxy-galaxy lensing profile. We note that our formalism allows different mask patterns between the shear and galaxy number density fields.

We have also investigated the covariance of the galaxy-shear cross spectrum using the ray-tracing simulations. We have found the excess covariance relative to the Gaussian error on large  $k$  where the shot noise is dominated in the Gaussian approximation. We have shown that the excess can be explained by the halo sample variance (HSV), which originates from matter fluctuations at scales larger than the survey area. In our examples, the HSV contribution increases the diagonal error of galaxy-galaxy lensing nearly twice at  $k \lesssim 1 h/\text{Mpc}$ , and also induces the off-diagonal elements. The HSV contribution has been ignored in previous galaxy-galaxy lensing analysis, and our results highlight the importance of including super survey modes in the covariance. We note that the Jackknife method does not contain information on fluctuations larger than the survey area, and thus substantially underestimates the HSV contribution. While we have included only the HSV term, more comprehensive analysis of the effect of the super sample covariance on galaxy-galaxy lensing is ongoing (Takada et al. in preparation).

We have applied the pseudo-spectrum method to the real observational dataset from the CFHTLenS shear catalogue and various spectroscopic samples including SDSS/LRG, BOSS/LOWZ, and BOSS/CMASS. We have detected the galaxy-shear cross spectra for all the three spectroscopic samples at the significance level of  $7 - 10\sigma$  by using the analytic covariance formulae including the HSV effect. We have confirmed that our galaxy-galaxy lensing measurements are consistent with the theoretical predictions based on the HOD model from previous work, which can be seen as a sanity check of our pseudo-spectrum method to measure the galaxy-galaxy lensing in the Fourier space. The methodology developed in this paper will be important for analyzing future data with which we will be able to measure galaxy-shear cross spectra out to larger scales.

## ACKNOWLEDGMENTS

We thank Masahiro Takada for fruitful discussions. This work was supported in part by World Premier International Research Center Initiative (WPI Initiative), MEXT, Japan, and JSPS KAKENHI Grant Number 26800093 and 15H05892.

## REFERENCES

Ahn C. P. et al., 2012, *ApJS*, 203, 21

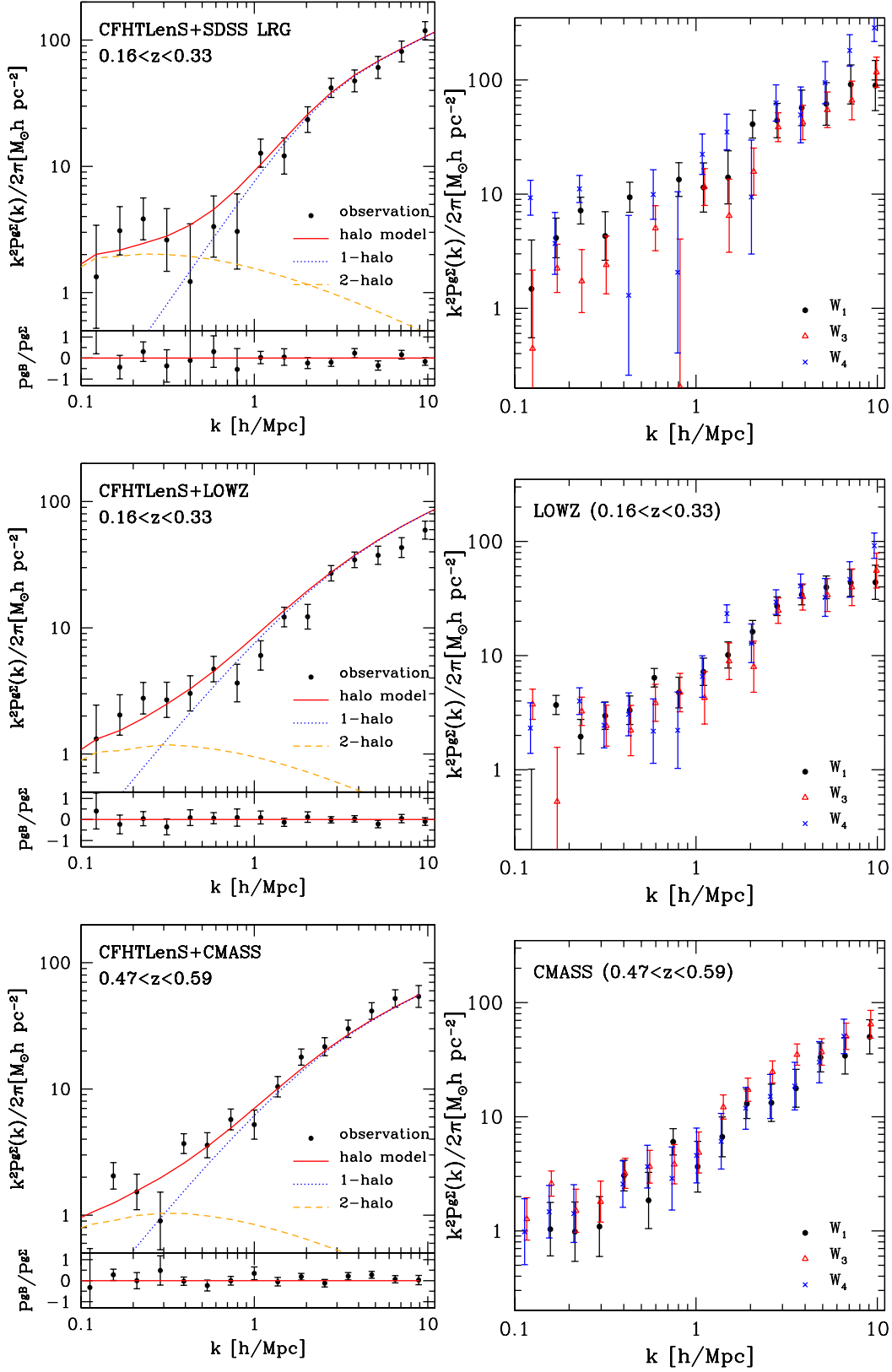


**Figure 5.** *Left:* Comparisons of the observed galaxy-shear cross spectra with the HOD model. From top to bottom, we show the results for SDSS/LRG, BOSS/LOWZ, and BOSS/CMASS. The HOD model parameters used here are summarized in Table 1. The one-halo term, two-halo term, and their sum are plotted with blue dotted, yellow dashed, and red solid lines, respectively. The observed cross spectra between the B-mode shear and galaxy density fields are also shown at the bottom panel of each figure. *Right:* The difference of the observed galaxy-shear cross spectra between three CFHTLenS fields ( $W_1, W_3, W_4$ ), again for the same three galaxy samples.

parameters	SDSS/LRG (Reid & Spergel 2009)	BOSS/LOWZ (Manera et al. 2015)	BOSS/CMASS (Manera et al. 2013)
cosmology	<i>WMAP3</i>	<i>WMAP7</i>	<i>WMAP7</i>
$\log_{10}(M_c)$	13.76	13.2	13.09
$\sigma_{\log M}$	0.7	0.62	0.60
$\log_{10}(M_0)$	13.54	13.24	13.08
$\log_{10}(M_1)$	14.54	14.32	14.00
$\alpha$	1.03	0.93	1.01
$\chi^2(\text{d.o.f.}=15)$	14.2	20.7	17.2

**Table 1.** The reference values of the 5 HOD parameters for the three spectroscopic samples, SDSS/LRGs (Reid & Spergel 2009), BOSS/CMASS, and LOWZ (Manera et al. 2013, 2015). The cosmology based on *WMAP* 3-year is assumed for the HOD parameter values of SDSS/LRGs, while the other HOD parameter values are based on *WMAP* 7-year (Komatsu et al. 2011). The unit of mass is  $h^{-1}M_\odot$ . The  $\chi^2$  values are obtained by comparing the HOD model predictions with the observed galaxy-shear cross spectra from 0.1h/Mpc to 10h/Mpc (15 bins of  $k$ ).

- Bartelmann M., Schneider P., 2001, *Phys. Report*, 340, 291  
Becker M. R., Rozo E., 2016, *MNRAS*, 457, 304  
Becker M. R. et al., 2016, *ArXiv e-prints arXiv:1507.05598*  
Benítez N., 2000, *ApJ*, 536, 571  
Brown M. L., Castro P. G., Taylor A. N., 2005, *MNRAS*, 360, 1262  
Brown M. L., Taylor A. N., Bacon D. J., Gray M. E., Dye S., Meisenheimer K., Wolf C., 2003, *MNRAS*, 341, 100  
Bunn E. F., Zaldarriaga M., Tegmark M., de Oliveira-Costa A., 2003, *Phys. Rev. D*, 67, 023501  
Coupon J. et al., 2015, *MNRAS*, 449, 1352  
Covone G., Sereno M., Kilbinger M., Cardone V. F., 2014, *ApJ*, 784, L25  
Dawson K. S. et al., 2013, *AJ*, 145, 10  
de Jong J. T. A. et al., 2015, *A.&Ap.*, 582, A62  
Duffy A. R., Schaye J., Kay S. T., Dalla Vecchia C., 2008, *MNRAS*, 390, L64  
Eisenstein D. J. et al., 2001, *AJ*, 122, 2267  
Eisenstein D. J. et al., 2011, *AJ*, 142, 72  
Erben T. et al., 2013, *MNRAS*, 433, 2545  
Grain J., Tristram M., Stomp R., 2009, *Phys. Rev. D*, 79, 123515  
Gruen D., Seitz S., Becker M. R., Friedrich O., Mana A., 2015, *MNRAS*, 449, 4264  
Hamana T., Mellier Y., 2001, *MNRAS*, 327, 169  
Heymans C. et al., 2013, *MNRAS*, 432, 2433  
Heymans C. et al., 2012, *MNRAS*, 427, 146  
Hikage C., Mandelbaum R., Takada M., Spergel D. N., 2013, *MNRAS*, 435, 2345  
Hikage C., Takada M., Hamana T., Spergel D., 2011, *MNRAS*, 412, 65  
Hildebrandt H. et al., 2012, *MNRAS*, 421, 2355  
Hivon E., Górski K. M., Netterfield C. B., Crill B. P., Prunet S., Hansen F., 2002, *ApJ*, 567, 2  
Hoekstra H., Hsieh B. C., Yee H. K. C., Lin H., Gladders M. D., 2005, *ApJ*, 635, 73  
Hu W., Jain B., 2004, *Phys. Rev. D*, 70, 043009  
Hu W., White M., 2001, *ApJ*, 554, 67  
Ivezic Z. et al., 2008, *ArXiv e-prints arXiv:0805.2366*  
Jain B., Seljak U., White S., 2000, *ApJ*, 530, 547  
Jee M. J., Tyson J. A., Schneider M. D., Wittman D., Schmidt S., Hilbert S., 2013, *ApJ*, 765, 74  
Jeong D., Komatsu E., Jain B., 2009, *Phys. Rev. D*, 80, 123527  
Kayo I., Takada M., Jain B., 2013, *MNRAS*, 429, 344  
Kilbinger M. et al., 2013, *MNRAS*, 430, 2200  
Kim J., Naselsky P., 2010, *A.&Ap.*, 519, A104  
Kitching T. D. et al., 2014, *MNRAS*, 442, 1326  
Kogut A. et al., 2003, *ApJS*, 148, 161  
Köhlinger F., Viola M., Valkenburg W., Joachimi B., Hoekstra H., Kuijken K., 2016, *MNRAS*, 456, 1508  
Komatsu E. et al., 2011, *ApJS*, 192, 18  
Laureijs R. et al., 2011, *ArXiv e-prints arXiv:1110.3193*  
Leauthaud A. et al., 2012, *ApJ*, 744, 159  
Levi M. et al., 2013, *ArXiv e-prints arXiv:1308.0847*  
Li Y., Hu W., Takada M., 2014, *Phys. Rev. D*, 89, 083519  
Limber D. N., 1954, *ApJ*, 119, 655  
Lin H. et al., 2012, *ApJ*, 761, 15  
Mandelbaum R., Seljak U., Kauffmann G., Hirata C. M., Brinkmann J., 2006, *MNRAS*, 368, 715  
Mandelbaum R., Slosar A., Baldauf T., Seljak U., Hirata C. M., Nakajima R., Reyes R., Smith R. E., 2013, *MNRAS*, 432, 1544  
Manera M. et al., 2015, *MNRAS*, 447, 437  
Manera M. et al., 2013, *MNRAS*, 428, 1036  
Miller L. et al., 2013, *MNRAS*, 429, 2858  
Miyatake H. et al., 2015, *ApJ*, 806, 1  
Miyatake H., More S., Takada M., Spergel D. N., Mandelbaum R., Rykoff E. S., Rozo E., 2016, *Physical Review Letters*, 116, 041301  
Miyazaki S. et al., 2012, in *SPIE*, Vol. 8446, Ground-based and Airborne Instrumentation for Astronomy IV, p. 84460Z  
Miyazaki S. et al., 2015, *ApJ*, 807, 22  
More S., Miyatake H., Mandelbaum R., Takada M., Spergel D. N., Brownstein J. R., Schneider D. P., 2015, *ApJ*, 806, 2  
Navarro J. F., Frenk C. S., White S. D. M., 1996, *ApJ*, 462, 563  
Oguri M., 2014, *MNRAS*, 444, 147  
Oguri M., Takada M., 2011, *Phys. Rev. D*, 83, 023008  
Reid B. A., Spergel D. N., 2009, *ApJ*, 698, 143  
Sato M., Hamana T., Takahashi R., Takada M., Yoshida N., Matsubara T., Sugiyama N., 2009, *ApJ*, 701, 945  
Sato M., Nishimichi T., 2013, *Phys. Rev. D*, 87, 123538  
Seljak U., 1998, *ApJ*, 506, 64  
Sereno M., Veropalumbo A., Marulli F., Covone G., Moscardini L., Cimatti A., 2015, *MNRAS*, 449, 4147  
Smith K. M., 2006, *Phys. Rev. D*, 74, 083002  
Smith K. M., Zaldarriaga M., 2007, *Phys. Rev. D*, 76, 043001  
Spergel D. et al., 2015, *ArXiv e-prints arXiv:1503.03757*  
Spergel D. N. et al., 2007, *ApJS*, 170, 377  
Takada M., Bridle S., 2007, *New Journal of Physics*, 9, 446  
Takada M. et al., 2014, *PASJ*, 66, 1

- Takada M., Hu W., 2013, Phys. Rev. D, 87, 123504  
 Takada M., Jain B., 2009, MNRAS, 395, 2065  
 The Dark Energy Survey Collaboration, 2005, ArXiv Astro-physics e-prints astro-ph/0510346  
 Tinker J., Kravtsov A. V., Klypin A., Abazajian K., Warren M., Yepes G., Gottlöber S., Holz D. E., 2008, ApJ, 688, 709  
 Tinker J. L., Robertson B. E., Kravtsov A. V., Klypin A., Warren M. S., Yepes G., Gottlöber S., 2010, ApJ, 724, 878  
 Umetsu K., Zitrin A., Gruen D., Merten J., Donahue M., Postman M., 2015, ArXiv e-prints arXiv:1507.04385  
 VanderPlas J. T., Connolly A. J., Jain B., Jarvis M., 2012, ApJ, 744, 180  
 Velander M. et al., 2014, MNRAS, 437, 2111  
 Wright C. O., Brainerd T. G., 2000, ApJ, 534, 34  
 Zheng Z., et al., 2005, ApJ, 633, 791

## APPENDIX A: FULL-SKY FORMALISM

In this Appendix, we provide the full-sky formalism for the pseudo-spectrum analysis of the shear power spectrum and galaxy-shear cross spectrum. This is analogous to the formalism developed for the CMB polarization and temperature cross spectrum (Hivon et al. 2002; Kogut et al. 2003; Brown et al. 2005).

The observed shear field  $\gamma$  can be decomposed into E-mode and B-mode shear by spherical harmonic transform with the spin-2 spherical harmonics  $\pm 2Y_{\ell m}$

$$\tilde{E}_{\ell m} \pm i\tilde{B}_{\ell m} = \int d\hat{n} \gamma(\hat{n}) \pm 2Y_{\ell m}^*(\hat{n}), \quad (\text{A1})$$

and the inverse relation is

$$\gamma(\hat{n}) = \sum_{\ell m} (\tilde{E}_{\ell m} \pm i\tilde{B}_{\ell m}) \pm 2Y_{\ell m}(\hat{n}). \quad (\text{A2})$$

The relation between the galaxy number density field and their Harmonic coefficients are given using the spin-0 spherical harmonics  ${}_0Y_{\ell m}$  as

$$\tilde{\delta}_{g,\ell m} = \int d\hat{n} \delta_g(\hat{n}) {}_0Y_{\ell m}^*(\hat{n}), \quad (\text{A3})$$

and

$$\delta_g(\hat{n}) = \sum_{\ell m} \tilde{\delta}_{g,\ell m} {}_0Y_{\ell m}(\hat{n}). \quad (\text{A4})$$

The effect of survey mask on the harmonic coefficients is expressed as their convolution

$$(\tilde{E}_{\ell m} \pm i\tilde{B}_{\ell m})^{(\text{obs})} = \int d\hat{n} U^\gamma(\hat{n}) \gamma(\hat{n}) \pm 2Y_{\ell m}^*(\hat{n}) \quad (\text{A5})$$

$$= \sum_{\ell' m'} (E_{\ell' m'} \pm iB_{\ell' m'})^{(\text{true})} \pm 2W_{\ell\ell' m m'}^\gamma \quad (\text{A6})$$

and

$$\tilde{\delta}_g^{(\text{obs})}(\hat{n}) = \int d\hat{n} U^g(\hat{n}) \delta_g(\hat{n}) {}_0Y_{\ell m}^*(\hat{n}) \quad (\text{A7})$$

$$= \sum_{\ell' m'} \tilde{\delta}_{g,\ell' m'}^{(\text{true})} {}_0W_{\ell\ell' m m'}^g, \quad (\text{A8})$$

and the convolution kernels are defined as

$${}_sW_{\ell\ell' m m'}^{g(\gamma)} \equiv \int d\hat{n} {}_sY_{\ell' m'}(\hat{n}) U^{g(\gamma)}(\hat{n}) {}_sY_{\ell m}^*(\hat{n})$$

$$= \sum_{\ell'' m''} \tilde{U}_{\ell'' m''}^{g(\gamma)} (-1)^m \sqrt{\frac{(2\ell+1)(2\ell'+1)(2\ell''+1)}{4\pi}} \times \begin{pmatrix} \ell & \ell' & \ell'' \\ s & -s & 0 \end{pmatrix} \begin{pmatrix} \ell & \ell' & \ell'' \\ m & m' & m'' \end{pmatrix}, \quad (\text{A9})$$

where  $\tilde{U}_{\ell m}^{g(\gamma)}$  represents the spherical harmonic transform of the mask field for galaxy overdensity field  $g$  or shear field  $\gamma$

$$\tilde{U}_{\ell m}^{g(\gamma)} = \int d\hat{n} U^{g(\gamma)}(\hat{n}) {}_0Y_{\ell m}^*(\hat{n}). \quad (\text{A10})$$

The auto and cross spectra are defined as

$$C_\ell^{XY} \equiv \frac{1}{2\ell+1} \sum_m \langle X_{\ell m} Y_{\ell m}^* \rangle, \quad (\text{A11})$$

where  $X$  and  $Y$  denotes  $E$ -mode shear,  $B$ -mode shear, and galaxy overdensity  $g$ . The pseudo spectra computed from the observed masked field are related to the true spectra as

$$\mathbf{C}_\ell^{(\text{obs})} = \sum_{\ell'} \mathbf{M}_{\ell\ell'} F_{\ell'}^2 \mathbf{C}_{\ell'}^{(\text{true})} + \mathbf{N}_\ell^{(\text{obs})}. \quad (\text{A12})$$

where  $\mathbf{C}$  denotes the 6-dimensional vector of power spectra for E-mode shear, B-mode shear, and galaxy overdensity and their cross spectra. Non-zero components of the mode coupling matrix  $\mathbf{M}_{\ell\ell'}$  are as follows:

$$\begin{aligned} M_{\ell\ell'}^{EE,EE} &= M_{\ell\ell'}^{BB,BB} \\ &= \frac{2\ell'+1}{8\pi} \sum_{\ell''} \mathcal{U}_{\ell'\ell''}^{\gamma\gamma} [1 + (-1)^{\ell+\ell'+\ell''}] \begin{pmatrix} \ell & \ell' & \ell'' \\ 2 & -2 & 0 \end{pmatrix}^2, \end{aligned} \quad (\text{A13})$$

$$\begin{aligned} M_{\ell\ell'}^{EE,BB} &= M_{\ell\ell'}^{BB,EE} \\ &= \frac{2\ell'+1}{8\pi} \sum_{\ell''} \mathcal{U}_{\ell'\ell''}^{\gamma\gamma} [1 - (-1)^{\ell+\ell'+\ell''}] \begin{pmatrix} \ell & \ell' & \ell'' \\ 2 & -2 & 0 \end{pmatrix}^2, \end{aligned} \quad (\text{A14})$$

$$M_{\ell\ell'}^{EB,EB} = \frac{2\ell'+1}{4\pi} \sum_{\ell''} \mathcal{U}_{\ell'\ell''}^{\gamma\gamma} \begin{pmatrix} \ell & \ell' & \ell'' \\ 2 & -2 & 0 \end{pmatrix}^2, \quad (\text{A15})$$

$$\begin{aligned} M_{\ell\ell'}^{gE,gE} &= M_{\ell\ell'}^{gB,gB} \\ &= \frac{2\ell'+1}{4\pi} \sum_{\ell''} \mathcal{U}_{\ell'\ell''}^{g\gamma} \begin{pmatrix} \ell & \ell' & \ell'' \\ 0 & 0 & 0 \end{pmatrix}^2 \begin{pmatrix} \ell & \ell' & \ell'' \\ 2 & -2 & 0 \end{pmatrix}^2, \end{aligned} \quad (\text{A16})$$

$$M_{\ell\ell'}^{gg,gg} = \frac{2\ell'+1}{4\pi} \sum_{\ell''} \mathcal{U}_{\ell'\ell''}^{gg} \begin{pmatrix} \ell & \ell' & \ell'' \\ 0 & 0 & 0 \end{pmatrix}^2. \quad (\text{A17})$$

where

$$\mathcal{U}_\ell^{XY} \equiv \frac{1}{2\ell+1} \sum_m \langle \tilde{U}_{\ell m}^X \tilde{U}_{\ell m}^{*Y} \rangle, \quad (\text{A18})$$

with  $X$  and  $Y$  being  $g$  or  $\gamma$ .